Author(s): Tuovinen, Toni & Hinkkanen, Marko

Title: Signal-Injection-Assisted Full-Order Observer With Parameter Adaptation for Synchronous Reluctance Motor Drives

Year: 2014

Version: Post print

Please cite the original version:

Tuovinen, Toni & Hinkkanen, Marko. 2014. Signal-Injection-Assisted Full-Order Observer With Parameter Adaptation for Synchronous Reluctance Motor Drives. IEEE Transactions on Industry Applications. Volume 50, Issue 5. 3392-3402. ISSN 0093-9994 (printed). DOI: 10.1109/tia.2014.2304588.

Signal-Injection Assisted Full-Order Observer With Parameter Adaptation for Synchronous Reluctance Motor Drives

Toni Tuovinen and Marko Hinkkanen, *Senior Member, IEEE*

***Abstract*—A back-EMF-based position observer for motion-sensorless synchronous reluctance motor (SyRM) drives is augmented with parameter-adaptation laws for improved operation at all speeds, including standstill. The augmented observer is theoretically analyzed under various operation conditions. The analysis indicates that the stator-resistance adaptation should be enabled only at low speeds, the d-axis inductance adaptation should be enabled only at medium and high speeds near no load, and the q-axis inductance adaptation should be enabled only at high speeds under high load. The augmented observer is experimentally evaluated using a 6.7-kW SyRM drive.**

***Index Terms*—Inductance adaptation, observer, parameter adaptation, parameter uncertainties, resistance adaptation, sensorless, signal injection, stability conditions.**

I. Introduction

The synchronous reluctance motor (SyRM) has recently reemerged as a contender to the induction motor in variable-speed drives [1]–[3]. As compared to the permanent-magnet synchronous motor (PMSM), the SyRM is magnetized from the stator winding, which renders field-weakening operation a straightforward procedure. The fluctuating price of rare-earth metals has also made the SyRM more favorable in relation to the PMSM.

In order to operate synchronous machines, the position of the rotor has to be either measured or estimated. Position-sensorless operation is commonly preferred. Estimation methods relying on the back electromotive force (EMF) fail to estimate the position at lowest speeds under load. However, as the SyRM is inherently salient, methods providing a rotor-position estimate even at standstill are readily applicable. These methods can be roughly categorized as: signal-injection methods [1], [3]–[6]; modified PWM [7], [8]; and methods based on stator current variation without additional signal [9], [10]. Since the signal-injection methods inflict additional noise and losses, back-EMF-based position estimation methods are a desirable starting point. At the lowest speeds, the underlying back-EMF-based observer can be augmented with additional information from a signal-injection based method [1], [11]–[14].

SyRMs are usually magnetically saturated in the rated operating point. The d-axis flux component saturates strongly as a function of the corresponding current component, and the d-axis saturation is coupled with the q-axis saturation. In this paper, the inductance estimates are adjusted using a back-EMF-based method for improved medium- and high-speed operation. The proposed inductance-adaptation method is intended to be used in an initialization test in order to obtain data of the operating-point inductances. This inductance data could then be stored in look-up tables, or a function-based saturation model could be fitted to this data in a fashion similar to [15]. Alternatively, if dynamic requirements of the application are moderate, the inductance-adaptation method could be applied during normal operation of the drive (instead of using look-up tables or a saturation model).

The stator resistance depends on the temperature. In this paper, the stator-resistance estimate of the underlying speed-adaptive full-order observer is adjusted on-line at low speeds using a high-frequency signal-injection method. This correction produced by the signal-injection method affects the estimation-error dynamics. Hence, additional focus has to be put on the tuning of the augmented observer, in order to avoid unstable regions and to guarantee smooth transitions between low and high speed regions. The augmented observer proposed in this paper is of a lower order than the method proposed in [13], where the information provided by the signal-injection method was used via introducing a fictitious speed-correction parameter, which was then utilized to update the resistance estimate. Reduction of the complexity of the observer simplifies the analysis and tuning procedure.

After a review of the motor model in Section II and the rotor-position observer in Section III, the main contributions of the paper are presented in Sections IV and V:

1) An adaptation law to adjust the inductance estimates at medium and high speeds using a back-EMF-based method is proposed.
2) Analytical equations for steady-state position-estimation and inductance-estimation errors are derived, taking into account the errors in the other parameter estimates. A stabilizing gain selection for the inductance adaptation is proposed based on the analytical stability conditions.
3) An adaptation law to adjust the stator-resistance estimate at low speeds using a signal-injection based method is proposed.
4) An analytical equation for steady-state resistance-estimation error is derived, and a stabilizing gain selection is proposed.

The experimental setup is described in Section VI, and performance of the proposed observer design is evaluated using laboratory experiments with a 6.7-kW SyRM drive in Section VII.

T. Tuovinen and M. Hinkkanen are with Aalto University, Department of Electrical Engineering, P.O. Box 13000, FI-00076 Aalto, Espoo, Finland (e-mail: toni.tuovinen@aalto.fi; marko.hinkkanen@aalto.fi).

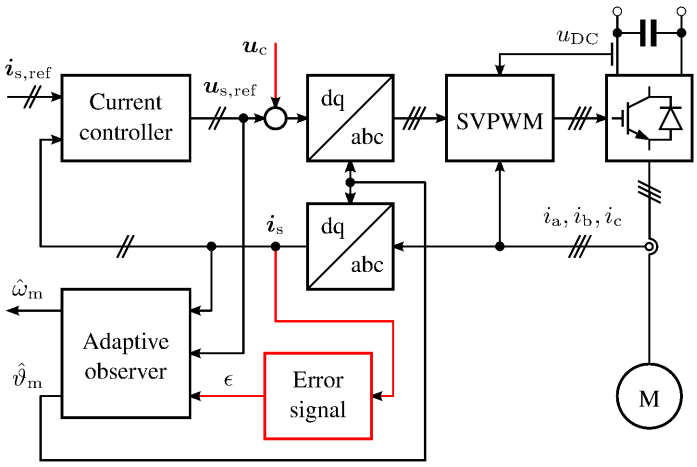

Fig. 1. Block diagram of the vector control system. The DC-link voltage u_{DC} and the phase currents i_{a}, i_{b}, and i_{c} are measured. The high-frequency voltage excitation $\boldsymbol{u}_{\mathrm{c}} = [u_{\mathrm{c}} \cos(\omega_{\mathrm{c}} t), 0]^{\mathrm{T}}$ is superimposed on the voltage reference. Dead-time effect and power-device voltage drops are compensated for in the space-vector modulator (SVPWM) using the phase-current feedback. The contents of the blocks "Adaptive observer" and "Error signal" are shown in Figs. 2(a) and 2(b), respectively.

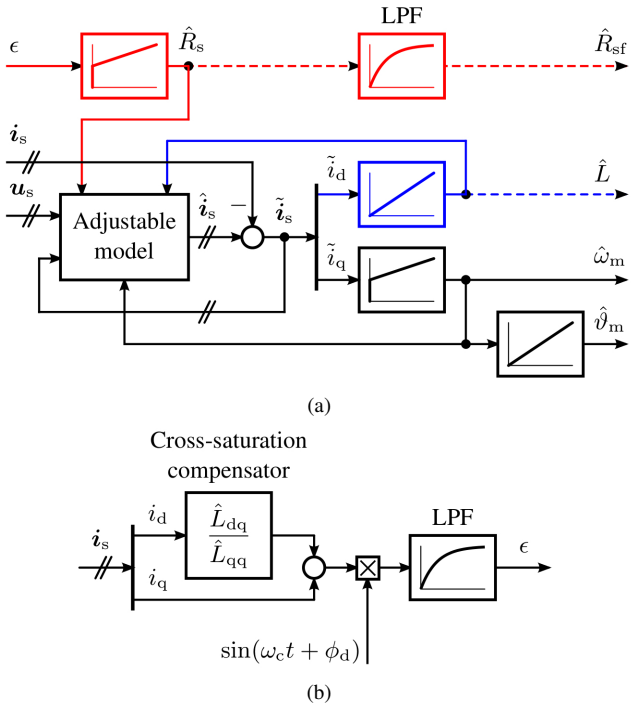

Fig. 2. (a) Adaptive observer. The adjustable model is defined in (5). The blue lines and blocks represent inductance adaptation, and the red lines and blocks represent resistance adaptation. (b) Error-signal calculation scheme. The bandwidth of the first-order low-pass filter (LPF) is α_{lp}. The effect of the discretization delay on the demodulation process is compensated for by means of the constant parameter ϕ_{d}.

II. SyRM Model

Real space vectors will be used here. For example, the stator-current vector is $\boldsymbol{i}_{\mathrm{s}} = [i_{\mathrm{d}}, i_{\mathrm{q}}]^{\mathrm{T}}$, where i_{d} and i_{q} are the components of the vector and the matrix transpose is marked with the superscript T. The orthogonal rotation matrix is defined as

$$\mathbf{J} = \begin{bmatrix} 0 & -1 \\ 1 & 0 \end{bmatrix}.$$

The electrical position of the d-axis is denoted by ϑ_{m}. The d-axis is defined as the direction of the maximum inductance of the rotor. The position depends on the electrical angular rotor speed ω_{m} according to

$$\frac{\mathrm{d}\vartheta_{\mathrm{m}}}{\mathrm{d}t} = \omega_{\mathrm{m}}. \tag{1}$$

To simplify the analysis in the following sections, the machine model will be expressed in the *estimated* rotor reference frame, whose d-axis is aligned at $\hat{\vartheta}_{\mathrm{m}}$ with respect to the stator reference frame. The stator inductance is

$$\boldsymbol{L} = \mathrm{e}^{-\tilde{\vartheta}_{\mathrm{m}}\mathbf{J}} \begin{bmatrix} L_{\mathrm{d}} & 0 \\ 0 & L_{\mathrm{q}} \end{bmatrix} \mathrm{e}^{\tilde{\vartheta}_{\mathrm{m}}\mathbf{J}} \tag{2}$$

where $\tilde{\vartheta}_{\mathrm{m}} = \hat{\vartheta}_{\mathrm{m}} - \vartheta_{\mathrm{m}}$ is the estimation error in the rotor position, L_{d} the direct-axis inductance, and L_{q} the quadrature-axis inductance. The voltage equation is

$$\frac{\mathrm{d}\boldsymbol{\psi}_{\mathrm{s}}}{\mathrm{d}t} = \boldsymbol{u}_{\mathrm{s}} - R_{\mathrm{s}}\boldsymbol{i}_{\mathrm{s}} - \hat{\omega}_{\mathrm{m}}\mathbf{J}\boldsymbol{\psi}_{\mathrm{s}} \tag{3a}$$

where $\boldsymbol{\psi}_{\mathrm{s}}$ is the stator-flux vector, $\boldsymbol{u}_{\mathrm{s}}$ the stator-voltage vector, R_{s} the stator resistance, and $\hat{\omega}_{\mathrm{m}} = \mathrm{d}\hat{\vartheta}_{\mathrm{m}}/\mathrm{d}t$ is the angular speed of the coordinate system. The stator current is a non-linear function

$$\boldsymbol{i}_{\mathrm{s}} = \boldsymbol{L}^{-1}\boldsymbol{\psi}_{\mathrm{s}} \tag{3b}$$

of the stator-flux vector and the position error $\tilde{\vartheta}_{\mathrm{m}}$.

III. Rotor-Position Observer

The block diagram of a sensorless vector-controlled SyRM drive is shown in Fig. 1. When the drive is operated in the speed-control mode, the control system is augmented with the speed controller, whose feedback signal is the rotor speed estimate $\hat{\omega}_{\mathrm{m}}$. In the following, the speed-adaptive full-order observer [16], [17] and the error-signal calculation are considered.

A. Speed-Adaptive Full-Order Observer

The speed-adaptive full-order observer is illustrated in Fig. 2(a). The dynamics of the rotor position estimate are given by

$$\frac{\mathrm{d}\hat{\vartheta}_{\mathrm{m}}}{\mathrm{d}t} = \hat{\omega}_{\mathrm{m}}. \tag{4}$$

In the adjustable model, the stator-flux vector and stator-current vector are estimated according to

$$\frac{\mathrm{d}\hat{\boldsymbol{\psi}}_{\mathrm{s}}}{\mathrm{d}t} = \boldsymbol{u}_{\mathrm{s}} - \hat{R}_{\mathrm{s}}\hat{\boldsymbol{i}}_{\mathrm{s}} - \hat{\omega}_{\mathrm{m}}\mathbf{J}\hat{\boldsymbol{\psi}}_{\mathrm{s}} + \boldsymbol{K}\tilde{\boldsymbol{i}}_{\mathrm{s}} \tag{5a}$$

$$\hat{\boldsymbol{i}}_{\mathrm{s}} = \hat{\boldsymbol{L}}^{-1}\hat{\boldsymbol{\psi}}_{\mathrm{s}} \tag{5b}$$

where $\hat{\boldsymbol{i}}_{\mathrm{s}}$ is the estimated stator-current vector, $\tilde{\boldsymbol{i}}_{\mathrm{s}} = \hat{\boldsymbol{i}}_{\mathrm{s}} - \boldsymbol{i}_{\mathrm{s}}$ is the estimation error of the stator current, $\boldsymbol{K}$ is the observer gain matrix, and $\hat{R}_{\mathrm{s}}$ is the stator resistance estimate. The inductance estimate matrix is

$$\hat{\boldsymbol{L}} = \begin{bmatrix} \hat{L}_{\mathrm{d}} & 0 \\ 0 & \hat{L}_{\mathrm{q}} \end{bmatrix} \tag{6}$$

where $\hat{L}_\mathrm{d}$ and $\hat{L}_\mathrm{q}$ are the direct-axis and quadrature-axis inductance estimates, respectively. Without loss of generality, the elements of the observer gain matrix are expressed as

$$\boldsymbol{K} = \begin{bmatrix} \hat{R}_\mathrm{s} + \hat{L}_\mathrm{d} k_{11} & \hat{L}_\mathrm{q} k_{12} \\ \hat{L}_\mathrm{d} k_{21} & \hat{R}_\mathrm{s} + \hat{L}_\mathrm{q} k_{22} \end{bmatrix} \tag{7}$$

in order to simplify the following equations. The four tuning parameters are k_{11}, k_{12}, k_{21}, and k_{22}. The rotor speed is estimated with the PI mechanism

$$\hat{\omega}_\mathrm{m} = \boldsymbol{k}_\mathrm{p} \tilde{\boldsymbol{i}}_\mathrm{s} + \int \boldsymbol{k}_\mathrm{i} \tilde{\boldsymbol{i}}_\mathrm{s} \mathrm{d}t. \tag{8}$$

The gain vectors $\boldsymbol{k}_\mathrm{p} = [0, k_\mathrm{p}]$ and $\boldsymbol{k}_\mathrm{i} = [0, k_\mathrm{i}]$ are chosen to utilize the estimation error only in the q-axis direction.

B. General Stabilizing Gain Design

In order to simplify the following analysis, the gains k_{12} and k_{22} are selected according to [18]

$$k_{12} = -\beta k_{11}, \quad k_{22} = -\beta k_{21} \tag{9}$$

where $\beta = i_\mathrm{q}/i_\mathrm{d}$. Locally stable estimation-error dynamics in every operating point are guaranteed for accurate model parameters, if the remaining elements of the observer gain matrix are selected as

$$k_{11} = k_1, \quad k_{21} = k_2 \tag{10}$$

where the functions k_1 and k_2 are

$$k_1 = -\frac{b + \beta(c/\hat{\omega}_\mathrm{m} - \hat{\omega}_\mathrm{m})}{\beta^2 + 1}, \quad k_2 = \frac{\beta b - c/\hat{\omega}_\mathrm{m} + \hat{\omega}_\mathrm{m}}{\beta^2 + 1}. \tag{11}$$

The new design parameters are b and c, which should be positive. In order to simplify the resulting equations, the speed-adaptation gains k_p and k_i are selected according to

$$k_\mathrm{p} = \frac{\hat{L}_\mathrm{q} d}{(\hat{L}_\mathrm{d} - \hat{L}_\mathrm{q}) i_\mathrm{d}}, \quad k_\mathrm{i} = \frac{\hat{L}_\mathrm{q} e}{(\hat{L}_\mathrm{d} - \hat{L}_\mathrm{q}) i_\mathrm{d}} \tag{12}$$

where d and e are design parameters, which may depend on the rotor speed. With this gain selection, the characteristic polynomial of the closed-loop system consisting of (1) – (12) can, after linearization, be split into a product of two second-order polynomials [18],

$$(s^2 + bs + c)(s^2 + ds + e) \tag{13}$$

and the stability is guaranteed for all positive values of b, c, d, and e, if the parameter estimates are accurate. It is worth noticing that the splitting of the characteristic polynomial in (13) originates from the selection (9). The observer is of the fourth order, and there are four gains. In order to further reduce the number of design parameters, d and e can be chosen as [18], [19]

$$d = 2\rho, \quad e = \rho^2 \tag{14}$$

yielding a double pole located at $s = -\rho$. The remaining three design parameters are b, c, and ρ, which should be positive.

IV. Inductance Adaptation

The proposed approach to adjust the inductance estimates is to use an adaptation law

$$\hat{L} = \int \boldsymbol{k}_\mathrm{L} \tilde{\boldsymbol{i}}_\mathrm{s} \mathrm{d}t \tag{15}$$

where the gain vector $\boldsymbol{k}_\mathrm{L} = [\hat{L}_\mathrm{d} k_\mathrm{L}, 0]$ is chosen to utilize the estimation error only in the d-axis direction. The gain vector is scaled by $\hat{L}_\mathrm{d}$ in order to simplify the following equations. The estimate $\hat{L}$ can be the d-axis inductance estimate $\hat{L}_\mathrm{d}$ or the q-axis inductance estimate $\hat{L}_\mathrm{q}$. The method is closely related to the permanent-magnet flux adaptation law proposed in [13]. The method is intended to be used in an initialization test in order to obtain data of the operating-point inductances for a saturation model. However, if dynamic requirements of the application are moderate, the inductance-adaptation method could also be applied during normal operation of the drive (instead of using a saturation model). In the following, only the key results are given, while the derivations can be found in the Appendix.

A. $\hat{L}_\mathrm{d}$ Is Adapted

1) Steady-State Errors: If the adaptation law (15), combined with the speed-adaptive full-order observer, is used to update the d-axis inductance estimate, it can be shown from (1) – (8) and (15) that the equation for the steady-state position error $\tilde{\vartheta}_\mathrm{m0}$ is (cf. Section B in the Appendix)

$$\begin{aligned} &(L_\mathrm{d} - L_\mathrm{q})\beta[\cos(2\tilde{\vartheta}_\mathrm{m0}) - 1] \\ &+ (L_\mathrm{d} - L_\mathrm{q})\sin(2\tilde{\vartheta}_\mathrm{m0}) + 2\tilde{L}_\mathrm{q}\beta - 2\tilde{R}_\mathrm{s}/\hat{\omega}_\mathrm{m} = 0 \end{aligned} \tag{16}$$

where $\tilde{R}_\mathrm{s} = \hat{R}_\mathrm{s} - R_\mathrm{s}$ is the resistance-estimation error and $\tilde{L}_\mathrm{q} = \hat{L}_\mathrm{q} - L_\mathrm{q}$ is the q-axis inductance-estimation error. The equation suggests that the position error is large when the load is large (because the effect of $\tilde{L}_\mathrm{q}$ is large) and when the speed of the motor is small (because the effect of $\tilde{R}_\mathrm{s}$ is large). Hence, the scheme should be used at high speeds and low loads.

The solution for the steady-state d-axis inductance estimate is

$$\begin{aligned} \hat{L}_\mathrm{d} =& \frac{L_\mathrm{d} - L_\mathrm{q}}{2}\cos(2\tilde{\vartheta}_\mathrm{m0}) - \beta\frac{L_\mathrm{d} - L_\mathrm{q}}{2}\sin(2\tilde{\vartheta}_\mathrm{m0}) \\ &+ \frac{L_\mathrm{d} + L_\mathrm{q}}{2} - \frac{\beta\tilde{R}_\mathrm{s}}{\hat{\omega}_\mathrm{m}}. \end{aligned} \tag{17}$$

Characteristic behaviour of the the worst-case d-axis inductance estimation error at different loads with parameter uncertainty is depicted in Fig. 3. The relative uncertainty of 20% is assumed for the parameter estimates $\hat{L}_\mathrm{q}$ and $\hat{R}_\mathrm{s}$. Hence, four different worst-case combinations, consisting of minimum and maximum values of the parameter estimates, can be formed. For example, one of the worst-case combinations is $\hat{L}_\mathrm{q} = 1.2L_\mathrm{q}$ and $\hat{R}_\mathrm{s} = 0.8R_\mathrm{s}$. At each studied operating point, the steady-state estimation errors of the system were evaluated for all four worst-case combinations of erroneous model parameters. It can be seen that the position error and the inductance-estimation error are large when the load is large.

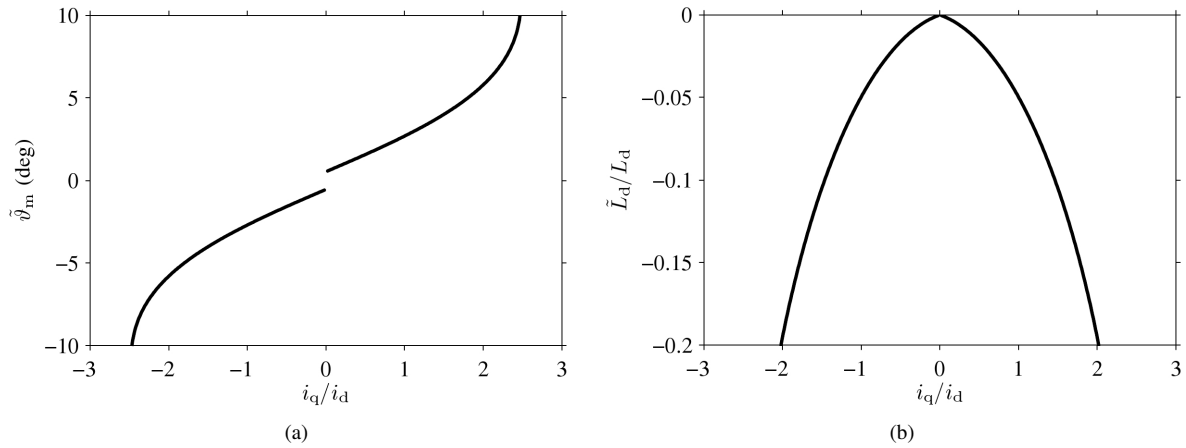

Fig. 3. Characteristic behaviour of the d-axis inductance adaptation at different loads with 20-% parameter uncertainty: (a) position estimation error; (b) inductance estimation error. The q-axis inductance is $L_\mathrm{q} = 0.3$ p.u., the stator resistance is $R_\mathrm{s} = 0.04$ p.u., and the speed is $\hat{\omega}_\mathrm{m} = 0.5$ p.u. Only the worst case is illustrated.

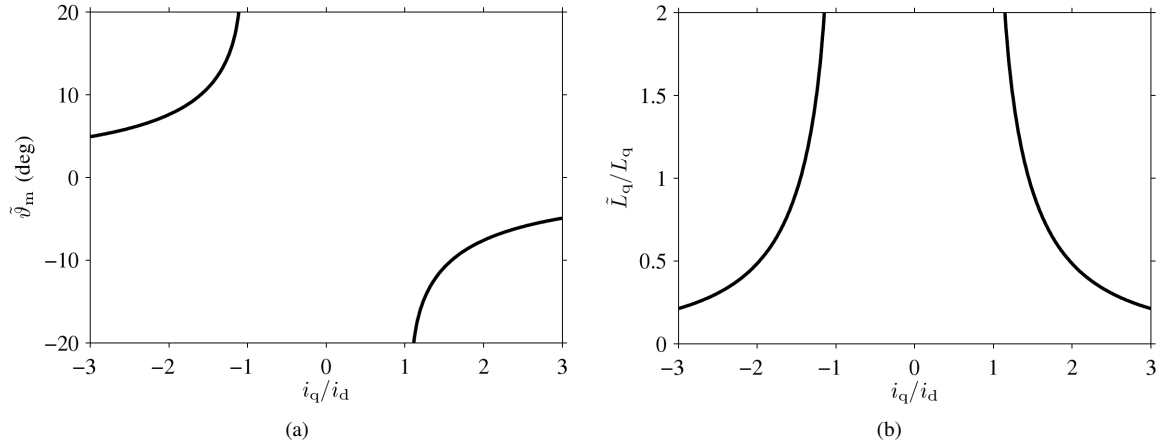

Fig. 4. Characteristic behaviour of the q-axis inductance adaptation at different loads with 20-% parameter uncertainty: (a) position estimation error; (b) inductance estimation error. The d-axis inductance is $L_\mathrm{d} = 2.0$ p.u., the stator resistance is $R_\mathrm{s} = 0.04$ p.u., and the speed is $\hat{\omega}_\mathrm{m} = 1$ p.u. Only the worst case is illustrated.

2) Gain Selection: The inductance adaptation (15) affects the dynamics of the closed-loop system slightly, and the tuning of the augmented observer has to be reconsidered. The gain selection (10) is lifted, and an alternative formulation for k_{11} and k_{21} is used, when the inductance adaptation is active.

It is assumed that the speed-adaptation loop (8) is faster than the inductance-adaptation loop and the flux observer. Under this assumption, the characteristic polynomial of the linearized closed-loop system consisting of (1) – (9) and (15) is (cf. Section C in the Appendix)

$$s^3 + A_2 s^2 + A_1 s + A_0 \tag{18a}$$

where

$$A_2 = \beta k_{21} - k_{11} + k_\mathrm{L} i_\mathrm{d} \tag{18b}$$

$$A_1 = -\hat{\omega}_\mathrm{m}\left(k_{21} - \hat{\omega}_\mathrm{m} + \beta k_{11}\right) \tag{18c}$$

$$A_0 = k_\mathrm{L} i_\mathrm{d} \hat{\omega}_\mathrm{m}^2. \tag{18d}$$

For design purposes, the characteristic polynomial is written in the form

$$(s^2 + bs + c)(s + \alpha_\mathrm{L}). \tag{19}$$

Equating (18) and (19), the gains of the augmented observer can be written as functions of the design parameters b, c, and α_L, which all should be positive in order to stabilize the system. When the d-axis inductance is adapted, the stabilizing observer gain selection with accurate $\hat{R}_\mathrm{s}$ and $\hat{L}_\mathrm{q}$ is

$$k_{11} = k_1 - \frac{k_2 \alpha_\mathrm{L}}{\hat{\omega}_\mathrm{m}}, \quad k_{21} = k_2 + \frac{k_1 \alpha_\mathrm{L}}{\hat{\omega}_\mathrm{m}} \tag{20}$$

where k_1 and k_2 are defined in (11). The adaptation gain is

$$k_\mathrm{L} = \frac{c\alpha_\mathrm{L}}{i_\mathrm{d} \hat{\omega}_\mathrm{m}^2}. \tag{21}$$

It is worth noticing that if the parameter α_L is small, the original selection (10) for k_{11} and k_{21} could be used.

B. $\hat{L}_\mathrm{q}$ Is Adapted

1) Steady-State Errors: If the adaptation law (15), combined with the speed-adaptive full-order observer, is used to update the q-axis inductance estimate, the position-error

equation is (cf. Section B in the Appendix)

$$\begin{aligned}&(L_\mathrm{d}-L_\mathrm{q})[\cos(2\tilde{\vartheta}_\mathrm{m0})-1]/\beta\\&-(L_\mathrm{d}-L_\mathrm{q})\sin(2\tilde{\vartheta}_\mathrm{m0})-2\tilde{L}_\mathrm{d}/\beta-2\tilde{R}_\mathrm{s}/\hat{\omega}_\mathrm{m}=0\end{aligned}\tag{22}$$

where $\tilde{L}_\mathrm{d}=\hat{L}_\mathrm{d}-L_\mathrm{d}$ is the d-axis inductance-estimation error. The equation suggests that the position error is large when the load is small (because the effect of $\tilde{L}_\mathrm{d}$ is large) and when the speed of the motor is small (because the effect of $\tilde{R}_\mathrm{s}$ is large). Hence, the scheme should be used at high speeds and high loads.

The solution for the steady-state q-axis inductance estimate is

$$\begin{aligned}\hat{L}_\mathrm{q}=&\frac{L_\mathrm{d}+L_\mathrm{q}}{2}-\frac{L_\mathrm{d}-L_\mathrm{q}}{2}\cos(2\tilde{\vartheta}_\mathrm{m0})\\&+\frac{\tilde{R}_\mathrm{s}}{\beta\hat{\omega}_\mathrm{m}}-\frac{L_\mathrm{d}-L_\mathrm{q}}{2\beta}\sin(2\tilde{\vartheta}_\mathrm{m0}).\end{aligned}\tag{23}$$

Characteristic behaviour of the worst-case q-axis inductance estimation error at different loads with parameter uncertainty of 20% is depicted in Fig. 4. It can be seen that the position error and the inductance-estimation error are large when the load is small.

2) Gain Selection: The stabilizing gain selection is derived in a fashion similar to previous subsection. The coefficients for (18) are (cf. Section C in the Appendix)

$$A_2=\beta k_{21}-k_{11}-k_\mathrm{L}i_\mathrm{d}\beta^2\tag{24}$$

$$A_1=-\hat{\omega}_\mathrm{m}\left(k_{21}-\hat{\omega}_\mathrm{m}+\beta k_{11}\right)\tag{25}$$

$$A_0=-k_\mathrm{L}i_\mathrm{d}\hat{\omega}_\mathrm{m}^2\beta^2.\tag{26}$$

When the q-axis inductance is adapted, the stabilizing gain selection with accurate $\hat{R}_\mathrm{s}$ and $\hat{L}_\mathrm{d}$ is determined by (20) and the adaptation gain is

$$k_\mathrm{L}=-\frac{c\alpha_\mathrm{L}}{\beta^2 i_\mathrm{d}\hat{\omega}_\mathrm{m}^2}.\tag{27}$$

V. Stator-Resistance Adaptation

A. High-Frequency Signal Injection

As shown in Fig. 1, a high-frequency voltage excitation is superimposed on the stator voltage in the estimated d-axis direction [20],

$$\boldsymbol{u}_\mathrm{c}=\begin{bmatrix}u_\mathrm{c}\cos(\omega_\mathrm{c}t)\\0\end{bmatrix}\tag{28}$$

where u_c and ω_c are the magnitude and the angular frequency, respectively, of the injected voltage. The high-frequency current responses depend on the position error,

$$i_\mathrm{dc}=\frac{u_\mathrm{c}\sin(\omega_\mathrm{c}t)}{\omega_\mathrm{c}L_\mathrm{det}}\Big[L_\Sigma-L_\Delta\cos(2\tilde{\vartheta}_\mathrm{m})-L_\mathrm{dq}\sin(2\tilde{\vartheta}_\mathrm{m})\Big]\tag{29a}$$

$$i_\mathrm{qc}=\frac{u_\mathrm{c}\sin(\omega_\mathrm{c}t)}{\omega_\mathrm{c}L_\mathrm{det}}\Big[L_\Delta\sin(2\tilde{\vartheta}_\mathrm{m})-L_\mathrm{dq}\cos(2\tilde{\vartheta}_\mathrm{m})\Big]\tag{29b}$$

where

$$L_\mathrm{det}=L_\mathrm{dd}L_\mathrm{qq}-L_\mathrm{dq}^2\tag{30a}$$

$$L_\Sigma=\frac{L_\mathrm{dd}+L_\mathrm{qq}}{2}\tag{30b}$$

$$L_\Delta=\frac{L_\mathrm{dd}-L_\mathrm{qq}}{2}\tag{30c}$$

and

$$L_\mathrm{dd}=\frac{\partial\psi_\mathrm{d}}{\partial i_\mathrm{d}},\quad L_\mathrm{dq}=\frac{\partial\psi_\mathrm{d}}{\partial i_\mathrm{q}},\quad L_\mathrm{qq}=\frac{\partial\psi_\mathrm{q}}{\partial i_\mathrm{q}}.\tag{30d}$$

The block diagram of the error-signal calculation is shown in Fig. 2(b). In order to compensate for the cross-saturation effects, the error signal ϵ is calculated using a combination of the d- and q-axis current components [21]. This combination is demodulated and low-pass filtered (LPF) [19], [22],

$$\epsilon=\mathrm{LPF}\left\{\left(\frac{\hat{L}_\mathrm{dq}}{\hat{L}_\mathrm{qq}}i_\mathrm{d}+i_\mathrm{q}\right)\sin(\omega_\mathrm{c}t+\phi_\mathrm{d})\right\}\tag{31}$$

where $\hat{L}_\mathrm{dq}$ is the estimated incremental inductance between the two axis and $\hat{L}_\mathrm{qq}$ is the estimated q-axis incremental inductance. The effect of the discretization delay on the demodulation process is compensated for by means of the constant parameter ϕ_d. A first-order low-pass filter is considered in the demodulation process.

Assuming accurate model parameters and small position error, the error signal ϵ in quasi-steady state reduces to [21]

$$\epsilon\approx k_\epsilon\sin(2\tilde{\vartheta}_\mathrm{m})\tag{32}$$

where k_ϵ is the signal-injection gain given by

$$k_\epsilon=\frac{u_\mathrm{c}}{\omega_\mathrm{c}}\frac{L_\Delta L_\mathrm{qq}-L_\mathrm{dq}^2}{2L_\mathrm{det}L_\mathrm{qq}}.\tag{33}$$

With accurate compensation factor $\hat{L}_\mathrm{dq}/\hat{L}_\mathrm{qq}$, the error signal ϵ vanishes with $\tilde{\vartheta}_\mathrm{m}=0$. Hence, the position error caused by the cross-saturation can be ideally reduced to zero if the ratio $\hat{L}_\mathrm{dq}/\hat{L}_\mathrm{qq}$ is known.

B. Proposed Adaptation Method

The proposed stator-resistance adaptation method is to feed the error signal ϵ obtained from (31) to the PI mechanism

$$\hat{R}_\mathrm{s}=\gamma_\mathrm{p}\epsilon+\int\gamma_\mathrm{i}\epsilon\mathrm{d}t.\tag{34}$$

When the resistance-adaptation mechanism is combined with the speed-adaptive full-order observer, it can be shown from (1) – (9) that the steady-state resistance-estimation error is (cf. Section B in the Appendix)

$$\tilde{R}_\mathrm{s}=\hat{\omega}_\mathrm{m}\frac{k_{11}\tilde{L}_\mathrm{d}+\tilde{L}_\mathrm{q}\beta(k_{21}-\hat{\omega}_\mathrm{m})}{k_{21}-\hat{\omega}_\mathrm{m}-\beta k_{11}}\tag{35}$$

where $\tilde{\vartheta}_\mathrm{m0}=0$ is assumed (corresponding to the assumption that the error signal ϵ produced by the signal-injection method is proportional to the position-estimation error). It can be seen that the resistance-estimation error is proportional to the rotor speed. Hence, the resistance adaptation should be disabled at higher speeds.

C. Proposed Gain Selection

The stator-resistance adaptation (34) affects the closed-loop estimation error dynamics, and the tuning of the augmented observer has to be reconsidered. The gain selection (10) is lifted, and an alternative formulation for k_{11} and k_{21} has to be used, when the stator-resistance adaptation is active.

It is assumed that the speed-adaptation loop (8) is faster than the resistance-adaptation loop and the flux observer. Under this assumption, the characteristic polynomial of the linearized closed-loop system consisting of (1) – (9) and (31) – (34) is (cf. Section C in the Appendix)

$$s^4 + A_3 s^3 + A_2 s^2 + A_1 s + A_0 \tag{36a}$$

where

$$A_3 = \alpha_{\mathrm{lp}} - k_{11} + \beta k_{21} \tag{36b}$$

$$A_2 = \frac{2k_\epsilon}{L_\mathrm{d} - L_\mathrm{q}} \alpha_{\mathrm{lp}} \beta \gamma_\mathrm{p} - \alpha_{\mathrm{lp}}(k_{11} - \beta k_{21}) - \hat{\omega}_\mathrm{m}(k_{21} - \hat{\omega}_\mathrm{m} + \beta k_{11}) \tag{36c}$$

$$A_1 = \frac{2k_\epsilon}{L_\mathrm{d} - L_\mathrm{q}} \alpha_{\mathrm{lp}} \left[\beta \gamma_\mathrm{i} + \gamma_\mathrm{p}(k_{21} - \hat{\omega}_\mathrm{m} - \beta k_{11})\right] - \alpha_{\mathrm{lp}} \hat{\omega}_\mathrm{m}(k_{21} - \hat{\omega}_\mathrm{m} + \beta k_{11}) \tag{36d}$$

$$A_0 = \frac{2k_\epsilon}{L_\mathrm{d} - L_\mathrm{q}} \alpha_{\mathrm{lp}} \gamma_\mathrm{i}(k_{21} - \hat{\omega}_\mathrm{m} - \beta k_{11}) \tag{36e}$$

and α_{lp} is the bandwidth of the low-pass filter in (31).

For design purposes, the characteristic polynomial is written as

$$(s^2 + bs + c)(s + \alpha'_{\mathrm{lp}})(s + \alpha_\mathrm{R}) \tag{37}$$

where b and c are design parameters associated with the flux observer. In the following, the design parameters α'_{lp} and α_R are associated with the low-pass filter (31) and the resistance-adaptation loop (34), respectively. The signal-injection can be turned off by selecting $\alpha_\mathrm{R} = 0$. Equating (36) and (37), the gains of the augmented observer can be written as functions of the design parameters $\{b, c, \alpha'_{\mathrm{lp}}, \alpha_\mathrm{R}\}$, which all should be positive in order to stabilize the system.

When b, c, α_R, and α_{lp} are the design parameters, the observer gain k_{11} is determined by

$$k_{11} = \beta k_{21} - b - \alpha_\mathrm{R} + \alpha_{\mathrm{lp}} - \alpha'_{\mathrm{lp}} \tag{38a}$$

and the resistance-adaptation gains γ_i and γ_p are

$$\gamma_\mathrm{i} = \frac{L_\mathrm{d} - L_\mathrm{q}}{2k_\epsilon} \frac{\alpha'_{\mathrm{lp}} \alpha_\mathrm{R} c}{\alpha_{\mathrm{lp}}(k_{21} - \hat{\omega}_\mathrm{m} - \beta k_{11})} \tag{38b}$$

$$\gamma_\mathrm{p} = \frac{L_\mathrm{d} - L_\mathrm{q}}{2k_\epsilon} \frac{\hat{\omega}_\mathrm{m}(k_{21} - \hat{\omega}_\mathrm{m} + \beta k_{11})}{k_{21} - \hat{\omega}_\mathrm{m} - \beta k_{11}} + \frac{L_\mathrm{d} - L_\mathrm{q}}{2k_\epsilon} \frac{\alpha'_{\mathrm{lp}}(c + b\alpha_\mathrm{R}) + c\alpha_\mathrm{R}}{\alpha_{\mathrm{lp}}(k_{21} - \hat{\omega}_\mathrm{m} - \beta k_{11})} - \frac{\beta \gamma_\mathrm{i}}{k_{21} - \hat{\omega}_\mathrm{m} - \beta k_{11}}. \tag{38c}$$

The remaining constraint from (36) and (37) is a cubic equation for either α'_{lp} or k_{21}. However, if the bandwidth α_{lp} of the low-pass filter in (31) is large, i.e. $\alpha_{\mathrm{lp}} \gg \alpha_\mathrm{R}$ and $\alpha_{\mathrm{lp}} \gg |-b \pm \sqrt{b^2 - 4c}|/2$, then approximation $\alpha'_{\mathrm{lp}} = \alpha_{\mathrm{lp}}$ can be used and k_{21} can be considered as a free variable. When $\alpha_\mathrm{R} \to 0$, then $k_{21} \to k_2$ should hold in accordance with (10), which also leads to $k_{11} \to k_1$.

VI. Experimental Setup and Implementation

The motion-sensorless control system, shown in Fig. 1, was implemented in a dSPACE DS1104 PPC/DSP board. A 6.7-kW four-pole SyRM was fed by a frequency converter that is controlled by the DS1104 board. The rated values of the SyRM are: speed 3175 r/min; frequency 105.8 Hz; line-to-line rms voltage 370 V; rms current 15.5 A; and torque 20.1 Nm. The base values for angular speed, voltage, and current are defined as $2\pi \cdot 105.8$ rad/s, $\sqrt{2/3} \cdot 370$ V, and $\sqrt{2} \cdot 15.5$ A, respectively.

A servo motor was used as a loading machine. The rotor speed ω_m and position ϑ_m were measured using an incremental encoder for monitoring purposes. The total moment of inertia of the experimental setup is 0.015 kgm^2 (2.7 times the inertia of the SyRM rotor).

The stator currents and the DC-link voltage were measured, and the reference voltage obtained from the current controller was used for the observer according to Fig. 1. The sampling was synchronized to the modulation, and both the switching frequency and the sampling frequency were 5 kHz. The effect of inverter nonlinearities on the stator voltage is substantial at low speeds. Therefore, the most significant inverter nonlinearities, i.e., the dead-time effect and power device voltage drops, have to be compensated for [23], [24]. Using phase a as an example, a compensated duty cycle for the pulsewidth modulator was evaluated as

$$d_\mathrm{a} = d_{\mathrm{a,ref}} + \frac{2d_\delta}{\pi} \arctan\left(\frac{i_\mathrm{a}}{i_\delta}\right) \tag{39}$$

where $d_{\mathrm{a,ref}}$ is the ideal duty cycle obtained from the current controller and i_a is the phase current. The parameter $d_\delta = 0.009$ p.u. takes into account both the dead-time effect and the threshold voltage of the power devices, while the on-state slope resistance of the power devices is included in the stator-resistance estimate. The shape of the arctan function is determined by the parameter $i_\delta = 0.014$ p.u. The duty cycles of phases b and c were evaluated in a similar manner.

The control system was augmented with a speed controller, whose feedback signal was the speed estimate $\hat{\omega}_\mathrm{m}$ obtained from the observer. The bandwidth of this PI controller, including active damping [25], was 0.05 p.u. The stator resistance estimate used in the inductance-adaptation tests is $\hat{R}_\mathrm{s} = 0.042$ p.u. (i.e., the measured dc resistance at room temperature).

The magnetic saturation has been modeled as functions of the estimated flux [26],

$$i_\mathrm{d} = \frac{\psi_\mathrm{d}}{L_{\mathrm{du}}} \left(1 + \alpha |\psi_\mathrm{d}|^k + \frac{\delta L_{\mathrm{du}}}{n+2} |\psi_\mathrm{d}|^m |\psi_\mathrm{q}|^{n+2}\right) \tag{40a}$$

$$i_\mathrm{q} = \frac{\psi_\mathrm{q}}{L_{\mathrm{qu}}} \left(1 + \gamma |\psi_\mathrm{q}|^l + \frac{\delta L_{\mathrm{qu}}}{m+2} |\psi_\mathrm{d}|^{m+2} |\psi_\mathrm{q}|^n\right) \tag{40b}$$

where $L_{\mathrm{du}} = 2.73$ p.u., $L_{\mathrm{qu}} = 0.843$ p.u., $\alpha = 0.333$ p.u., $\gamma = 5.58$ p.u., $\delta = 2.60$ p.u., $k = 6.6$, $l = 0.8$, $m = 1$, and $n = 0$. The constant d-axis current reference $i_{\mathrm{d,ref}} = 0.4$ p.u. is used.

A smooth transition from standstill to high-speed operation is implemented by decreasing the injected voltage as the speed increases,

$$u_{\mathrm{c}} = u_{\mathrm{c0}} f(\hat{\omega}_{\mathrm{m}}) \tag{41}$$

where the transition function is

$$f(\hat{\omega}_{\mathrm{m}}) = \begin{cases} 1 - \left| \frac{\hat{\omega}_{\mathrm{m}}}{\omega_\Delta} \right|, & \text{if } |\hat{\omega}_{\mathrm{m}}| \leq \omega_\Delta \\ 0, & \text{otherwise} \end{cases} \tag{42}$$

and $u_{\mathrm{c0}} = 0.1$ p.u. and $\omega_\Delta = 0.1$ p.u.

The design parameter b is chosen according to

$$b = \begin{cases} \omega_\Delta, & \text{if } |\hat{\omega}_{\mathrm{m}}| \leq \omega_\Delta \\ |\hat{\omega}_{\mathrm{m}}|, & \text{otherwise.} \end{cases} \tag{43}$$

Other design parameters values were: $c = 2.0 \cdot b^2$, $\omega_{\mathrm{c}} = 2\pi \cdot 500$ rad/s, $\alpha_{\mathrm{lp}} = 0.3$ p.u., $\alpha_{\mathrm{R}} = 0.02$ p.u.$\cdot f(\hat{\omega}_{\mathrm{m}})$, and $\rho = 2$ p.u. The gain selection was based on (38) and k_{21} was selected according to

$$k_{21} = \frac{\beta(b + \alpha_{\mathrm{R}}) + \hat{\omega}_{\mathrm{m}}}{\beta^2 + 1} - \frac{c\hat{\omega}_{\mathrm{m}}}{\omega_\Delta^2(\beta^2 + 1)} \tag{44}$$

when $|\hat{\omega}_{\mathrm{m}}| < \omega_\Delta$, which reduces to (10) when $\alpha_{\mathrm{R}} \to 0$ and $|\hat{\omega}_{\mathrm{m}}| \to \omega_\Delta$.

The resistance estimate $\hat{R}_{\mathrm{sf}}$ seen by the remaining parts of the system, such as the current controller, is obtained using a 0.5-Hz low-pass filter for the internal resistance estimate $\hat{R}_{\mathrm{s}}$ of the flux observer. The compensation for cross saturation is modeled as

$$\frac{\hat{L}_{\mathrm{dq}}}{\hat{L}_{\mathrm{qq}}} = -0.45 \cdot \frac{2}{\pi} \arctan\left(\frac{i_{\mathrm{q}}}{0.2 \text{ p.u.}} \right). \tag{45}$$

VII. Simulation and Experimental Results

A. Inductance Adaptation

Simulation results of inductance adaptation in no-load condition are depicted in Fig. 5(a). The speed reference is $\omega_{\mathrm{m,ref}} = 0.5$ p.u. The adaptation is turned on at $t = 1$ s with adaptation parameter $\alpha_{\mathrm{L}} = 0.1$ p.u. and initial value $\hat{L}_{\mathrm{d}} = 2.0$ p.u. It can be seen that the estimated inductance converges to the actual value, and the position error decreases simultaneously.

Similar results for the experimental setup are depicted in Fig. 5(b). Since the actual machine saturates, the initial value of the actual inductance is slightly larger than the final value due to position error. In this experiment, the q-axis inductance estimate is $\hat{L}_{\mathrm{q}} = 0.45$ p.u. The final value of the estimated inductance coincides with the mean value of the actual inductance, and the mean value of the position error is close to zero. If the bandwidth of the inductance adaptation were increased, the inductance estimate would follow the inductance harmonics (which is typically undesirable).

Experimental results of the q-axis inductance adaptation with load-torque step are depicted in Fig. 6. Initially, the rated load torque was applied. The adaptation is turned on at $t = 1$ s with adaptation parameter $\alpha_{\mathrm{L}} = 0.1$ p.u. and initial value $\hat{L}_{\mathrm{q}} = 0.45$ p.u. In this experiment, the d-axis inductance estimate is $\hat{L}_{\mathrm{d}} = 1.92$ p.u. The load torque was reversed at $t =$ 4.0 s. The speed reference is $\omega_{\mathrm{m,ref}} = 0.5$ p.u. It can be seen that the position error decreases close to zero. The adapted q-axis inductance differs from the value given by the inductance model due to error in the (constant) d-axis inductance estimate.

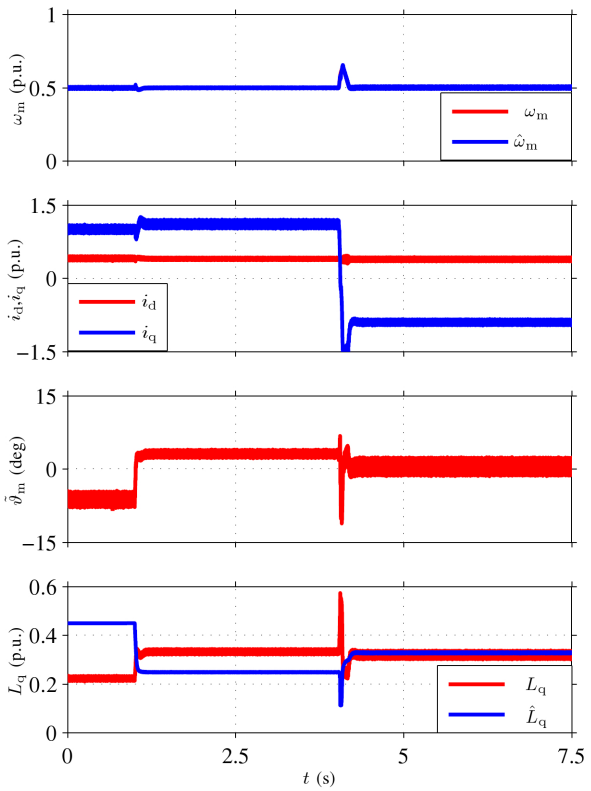

Fig. 6. Experimental results of the q-axis inductance adaptation with load-torque step (positive rated → negative rated). The speed reference is $\omega_{\mathrm{m,ref}} = 0.5$ p.u. The adaptation is turned on at $t = 1$ s.

B. Resistance Adaptation

Experimental results of the resistance adaptation with load-torque steps when the speed reference was kept at 0 are shown in Fig. 7. Initially, the negative rated load torque was applied at $\hat{\omega}_{\mathrm{m}} = 0.1$ p.u. The drive was decelerated to standstill at $t = 1$ s. The load torque was reversed at $t = 5.0$ s and reversed again at $t = 7.5$ s. It can be seen that the filtered resistance estimate in the third subplot recovers rapidly from a sudden load reversal, and the variation is nearly independent of the sign of the load. The small variation originates from the fact that in the analysis it was assumed that the steady-state position error is zero, which is not actually the case.

Experimental results of sloped speed reversals from $\hat{\omega}_{\mathrm{m}} = 0.1$ p.u. to $\hat{\omega}_{\mathrm{m}} = -0.1$ p.u. and then back to $\hat{\omega}_{\mathrm{m}} = 0.1$ p.u. under the negative rated load torque are shown in Fig. 8. In Fig. 8(a), the resistance adaptation has been disabled. In Fig. 8(b), the adaptation has been enabled. It can be seen that the drive is unstable in the vicinity of zero speed without the resistance adaptation.

The filtered resistance estimate in the third subplot varies with the speed, as predicted by (35), but the variation remains small. The noise in the estimates originates from saturation-induces saliencies (second harmonic), which is seen as a speed

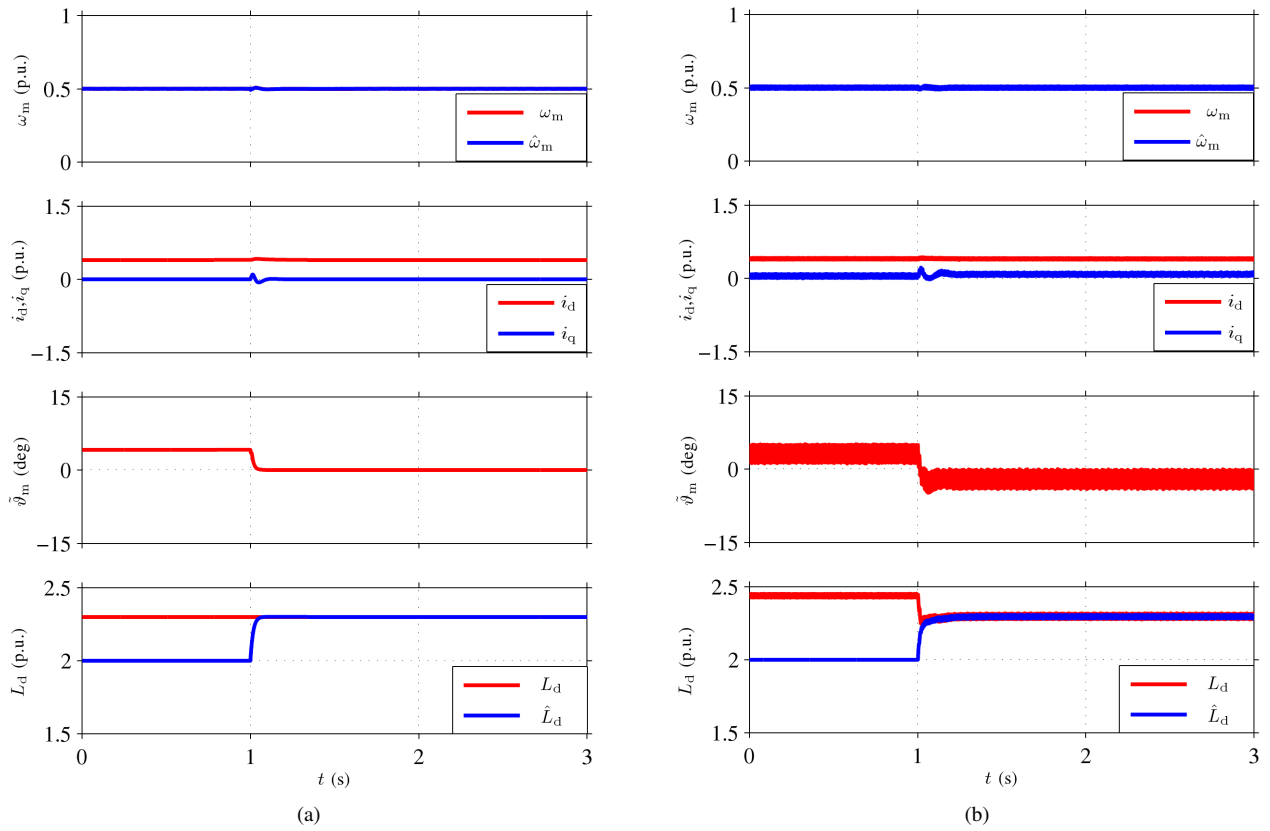

(a) (b)

Fig. 5. Adaptation of the d-axis inductance adaptation in no-load condition: (a) simulation results; (b) experimental results. The speed reference is $\omega_{\mathrm{m,ref}} = 0.5$ p.u. The adaptation is turned on at $t = 1$ s.

deviation by the speed controller and thus amplified. The noise disappears as the speed approaches zero.

The actual behaviour of the resistance estimate (34) in Fig. 8(b), when the speed is $\hat{\omega}_\mathrm{m} \approx -0.05$ p.u., is shown in Fig. 9. The solid line shows the actual resistance estimate $\hat{R}_\mathrm{s}$ and the dashed line shows the filtered estimate $\hat{R}_\mathrm{sf}$ seen by remaining parts of the system, such as the current controller. It can be seen that the resistance estimate varies with twice the rotational frequency. Hence, the resistance estimate (34) should be considered as an internal compensation variable and the filtered resistance estimate represents the actual resistance.

VIII. Conclusions

In this paper, a speed-adaptive full-order observer is augmented with parameter-adaptation laws for SyRM drives. The inductances are adapted using a back-EMF-based method, and the stator resistance is adapted using a signal-injection method. The analytical equations for steady-state estimation errors indicate that the resistance adaptation should be enabled only at low speeds, the d-axis inductance adaptation should be enabled only at medium and high speeds near no load, and the q-axis inductance adaptation should be enabled only at high speeds under high loads. The methods perform well under the intended operation conditions, and both small position error and small parameter estimation errors are demonstrated in laboratory experiments.

Acknowledgment

The authors gratefully acknowledge ABB Oy for the financial support.

Appendix
Estimation Errors

First, nonlinear closed-loop estimation-error dynamics relating to the augmented observer are given as a starting point. Then, the equations for steady-state estimation errors are given. Finally, the linearized models for the estimation-error dynamics are shown.

A. Nonlinear Estimation-Error Dynamics

The nonlinear estimation-error dynamics of the closed-loop system, consisting of (3) and (5), are

$$\begin{aligned}\frac{\mathrm{d}\tilde{\boldsymbol{\psi}}_\mathrm{s}}{\mathrm{d}t} &= \left[\left(\boldsymbol{K} - \hat{R}_\mathrm{s}\mathbf{I}\right)\hat{\boldsymbol{L}}^{-1} - \hat{\omega}_\mathrm{m}\mathbf{J}\right]\tilde{\boldsymbol{\psi}}_\mathrm{s} \\ &\quad + \left[\left(\boldsymbol{K} - \hat{R}_\mathrm{s}\mathbf{I}\right)\left(\hat{\boldsymbol{L}}^{-1}\boldsymbol{L} - \mathbf{I}\right) - \tilde{R}_\mathrm{s}\mathbf{I}\right]\boldsymbol{i}_\mathrm{s} \qquad (46a)\\ \tilde{\boldsymbol{i}}_\mathrm{s} &= \hat{\boldsymbol{L}}^{-1}\tilde{\boldsymbol{\psi}}_\mathrm{s} + \left(\hat{\boldsymbol{L}}^{-1}\boldsymbol{L} - \mathbf{I}\right)\boldsymbol{i}_\mathrm{s} \qquad (46b)\end{aligned}$$

where $\tilde{\boldsymbol{\psi}}_\mathrm{s} = \hat{\boldsymbol{\psi}}_\mathrm{s} - \boldsymbol{\psi}_\mathrm{s}$. The inductance matrix $\boldsymbol{L}$, defined in (2), is a function of the position estimation error $\tilde{\vartheta}_\mathrm{m}$, whose dynamics are

$$\frac{\mathrm{d}\tilde{\vartheta}_\mathrm{m}}{\mathrm{d}t} = \tilde{\omega}_\mathrm{m} \qquad (47)$$

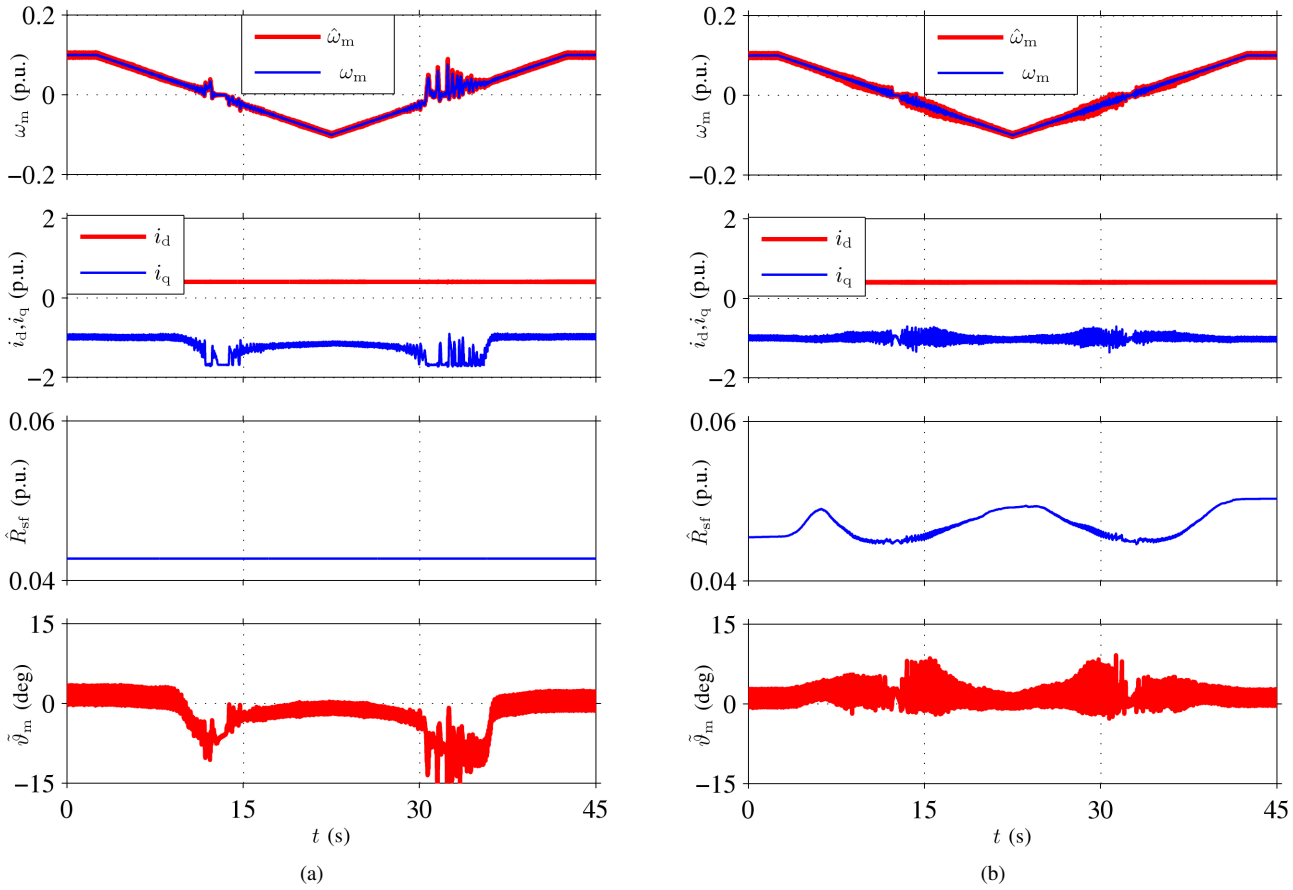

Fig. 8. Experimental results of sloped speed reversals ($\hat{\omega}_\mathrm{m} = 0.1$ p.u. $\rightarrow \hat{\omega}_\mathrm{m} = -0.1$ p.u. $\rightarrow \hat{\omega}_\mathrm{m} = 0.1$ p.u.) under the negative rated load torque: (a) without the resistance adaptation; (b) with the resistance adaptation.

according to (1) and (4). The dynamics of the speed-estimation error $\tilde{\omega}_\mathrm{m} = \hat{\omega}_\mathrm{m} - \omega_\mathrm{m}$ are

$$\frac{\mathrm{d}\tilde{\omega}_\mathrm{m}}{\mathrm{d}t} = \boldsymbol{k}_\mathrm{i}\tilde{\boldsymbol{i}}_\mathrm{s} + \frac{\mathrm{d}}{\mathrm{d}t}(\boldsymbol{k}_\mathrm{p}\tilde{\boldsymbol{i}}_\mathrm{s}) \tag{48}$$

based on (8). Similarly, the dynamics of the inductance-estimation error $\tilde{L} = \hat{L} - L$ are

$$\frac{\mathrm{d}\tilde{L}}{\mathrm{d}t} = \boldsymbol{k}_\mathrm{L}\tilde{\boldsymbol{i}}_\mathrm{s} \tag{49}$$

based on (15).

B. Steady-State Estimation Errors

The flux-estimation error in steady state can be solved from (46a). If the gains are selected according to (9), the flux-estimation errors are

$$\tilde{\psi}_\mathrm{d0} = -\frac{i_\mathrm{d}k_{21}(\beta^2+1)(L_\mathrm{d}-L_\mathrm{q})[\cos(2\tilde{\vartheta}_\mathrm{m0})-1]}{2(k_{21}-\hat{\omega}_\mathrm{m}+\beta k_{11})} + i_\mathrm{d}\frac{\beta(k_{21}+\hat{\omega}_\mathrm{m}-\beta k_{11})\tilde{R}_\mathrm{s} + k_{21}\hat{\omega}_\mathrm{m}(\tilde{L}_\mathrm{d}-\beta^2\tilde{L}_\mathrm{q})}{\hat{\omega}_\mathrm{m}(k_{21}-\hat{\omega}_\mathrm{m}+\beta k_{11})} \tag{50a}$$

$$\tilde{\psi}_\mathrm{q0} = \frac{i_\mathrm{d}k_{11}(\beta^2+1)(L_\mathrm{d}-L_\mathrm{q})[\cos(2\tilde{\vartheta}_\mathrm{m0})-1]}{2(k_{21}-\hat{\omega}_\mathrm{m}+\beta k_{11})} - i_\mathrm{d}\frac{(\hat{\omega}_\mathrm{m}-k_{21}+\beta k_{11})\tilde{R}_\mathrm{s} + k_{11}\hat{\omega}_\mathrm{m}(\tilde{L}_\mathrm{d}-\beta^2\tilde{L}_\mathrm{q})}{\hat{\omega}_\mathrm{m}(k_{21}-\hat{\omega}_\mathrm{m}+\beta k_{11})} \tag{50b}$$

Naturally, the flux estimation error is zero, if accurate parameter estimates are assumed. The steady-state position-estimation error can be solved from (48) after the steady-state flux-estimation errors are solved,

$$A\cos(2\tilde{\vartheta}_\mathrm{m0}) + B\sin(2\tilde{\vartheta}_\mathrm{m0}) + C = 0 \tag{51a}$$

where

$$A = (L_\mathrm{d}-L_\mathrm{q})\left[\beta(k_{21}-\hat{\omega}_\mathrm{m})-k_{11}\right] \tag{51b}$$

$$B = (L_\mathrm{d}-L_\mathrm{q})\left[(k_{21}-\hat{\omega}_\mathrm{m})+\beta k_{11}\right] \tag{51c}$$

$$C = -A + 2[\beta k_{11} - (k_{21}-\hat{\omega}_\mathrm{m})]\tilde{R}_\mathrm{s}/\hat{\omega}_\mathrm{m} + 2k_{11}\tilde{L}_\mathrm{d} + 2\beta(k_{21}-\hat{\omega}_\mathrm{m})\tilde{L}_\mathrm{q}. \tag{51d}$$

$$\frac{\mathrm{d}}{\mathrm{d}t}\begin{bmatrix}\tilde{\psi}_\mathrm{d}\\ \tilde{\psi}_\mathrm{q}\\ \tilde{\vartheta}_\mathrm{m}\\ \tilde{\omega}_\mathrm{m}\\ \tilde{L}_\mathrm{d}\end{bmatrix}=\begin{bmatrix} k_{11} & k_{12}+\hat{\omega}_\mathrm{m} & a_{13} & \tilde{\psi}_{\mathrm{q}0} & -k_{11}i_\mathrm{d}\\ k_{21}-\hat{\omega}_\mathrm{m} & k_{22} & a_{23} & -\tilde{\psi}_{\mathrm{d}0} & -k_{21}i_\mathrm{d}\\ 0 & 0 & 0 & 1 & 0\\ a_{41} & a_{42} & a_{43} & a_{44} & -\frac{dk_{21}}{\hat{L}_\mathrm{d}-\hat{L}_\mathrm{q}}\\ k_\mathrm{L} & 0 & -k_\mathrm{L}\beta_\mathrm{num} & 0 & -k_\mathrm{L}\frac{\beta_\mathrm{den}+2\tilde{\psi}_{\mathrm{d}0}+(L_\mathrm{d}+L_\mathrm{q})i_\mathrm{d}}{2\hat{L}_\mathrm{d}}\end{bmatrix}\begin{bmatrix}\tilde{\psi}_\mathrm{d}\\ \tilde{\psi}_\mathrm{q}\\ \tilde{\vartheta}_\mathrm{m}\\ \tilde{\omega}_\mathrm{m}\\ \tilde{L}_\mathrm{d}\end{bmatrix} \tag{53}$$

$$\frac{\mathrm{d}}{\mathrm{d}t}\begin{bmatrix}\tilde{\psi}_\mathrm{d}\\ \tilde{\psi}_\mathrm{q}\\ \tilde{\vartheta}_\mathrm{m}\\ \tilde{\omega}_\mathrm{m}\\ \tilde{R}_\mathrm{s}\\ \tilde{\epsilon}\end{bmatrix}=\begin{bmatrix} k_{11} & k_{12}+\hat{\omega}_\mathrm{m} & a_{13} & \tilde{\psi}_{\mathrm{q}0} & -i_\mathrm{d} & 0\\ k_{21}-\hat{\omega}_\mathrm{m} & k_{22} & a_{23} & -\tilde{\psi}_{\mathrm{d}0} & -i_\mathrm{q} & 0\\ 0 & 0 & 0 & 1 & 0 & 0\\ a_{41} & a_{42} & a_{43} & a_{44} & a_{45} & 0\\ 0 & 0 & 2\gamma_\mathrm{p}\alpha_\mathrm{lp}k_\epsilon & 0 & 0 & \gamma_\mathrm{i}-\gamma_\mathrm{p}\alpha_\mathrm{lp}\\ 0 & 0 & 2\alpha_\mathrm{lp}k_\epsilon & 0 & 0 & -\alpha_\mathrm{lp}\end{bmatrix}\begin{bmatrix}\tilde{\psi}_\mathrm{d}\\ \tilde{\psi}_\mathrm{q}\\ \tilde{\vartheta}_\mathrm{m}\\ \tilde{\omega}_\mathrm{m}\\ \tilde{R}_\mathrm{s}\\ \tilde{\epsilon}\end{bmatrix} \tag{56}$$

$$\frac{\mathrm{d}}{\mathrm{d}t}\begin{bmatrix}\tilde{\psi}_\mathrm{d}\\ \tilde{\psi}_\mathrm{q}\\ \tilde{R}_\mathrm{s}\\ \tilde{\epsilon}\end{bmatrix}=\begin{bmatrix} k_{11} & k_{12}+\hat{\omega}_\mathrm{m}+\frac{a_{13}}{(L_\mathrm{d}-L_\mathrm{q})i_\mathrm{d}} & -i_\mathrm{d} & 0\\ k_{21}-\hat{\omega}_\mathrm{m} & k_{22}+\frac{a_{23}}{(L_\mathrm{d}-L_\mathrm{q})i_\mathrm{d}} & -i_\mathrm{q} & 0\\ 0 & \frac{2k_\epsilon\alpha_\mathrm{lp}\gamma_\mathrm{p}}{(L_\mathrm{d}-L_\mathrm{q})i_\mathrm{d}} & 0 & \gamma_\mathrm{i}-\alpha_\mathrm{lp}\gamma_\mathrm{p}\\ 0 & \frac{2k_\epsilon\alpha_\mathrm{lp}}{(L_\mathrm{d}-L_\mathrm{q})i_\mathrm{d}} & 0 & -\alpha_\mathrm{lp}\end{bmatrix}\begin{bmatrix}\tilde{\psi}_\mathrm{d}\\ \tilde{\psi}_\mathrm{q}\\ \tilde{R}_\mathrm{s}\\ \tilde{\epsilon}\end{bmatrix} \tag{57}$$

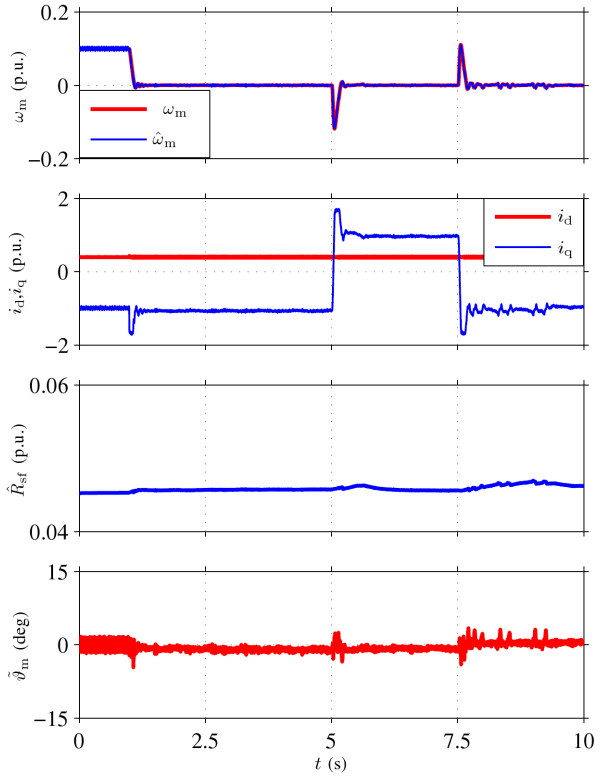

Fig. 7. Experimental results of the stator-resistance estimation with load-torque steps (negative rated → rated → negative rated) when the speed reference is kept at 0. The drive was decelerated to standstill at $t = 1$ s from $\hat{\omega}_\mathrm{m} = 0.1$ p.u.

From (49), an additional constraint is obtained for the position-estimation error in the steady state:

$$\begin{aligned}&(L_\mathrm{d}-L_\mathrm{q})[1-\cos(2\tilde{\vartheta}_{\mathrm{m}0})+\beta\sin(2\tilde{\vartheta}_{\mathrm{m}0})]\\&\quad+2\tilde{L}_\mathrm{d}+2\beta\tilde{R}_\mathrm{s}/\hat{\omega}_\mathrm{m}=0.\end{aligned} \tag{52}$$

Together with (51), this determines $\tilde{L}_\mathrm{d}$ and $\tilde{\vartheta}_{\mathrm{m}0}$ when the d-axis inductance is adapted, or $\tilde{L}_\mathrm{q}$ and $\tilde{\vartheta}_{\mathrm{m}0}$ when the q-axis inductance is adapted. If the stator resistance is updated using the signal injection, the additional constraint with accurate compensation is $\tilde{\vartheta}_{\mathrm{m}0}=0$, and $\tilde{R}_\mathrm{s}$ can be solved from (51).

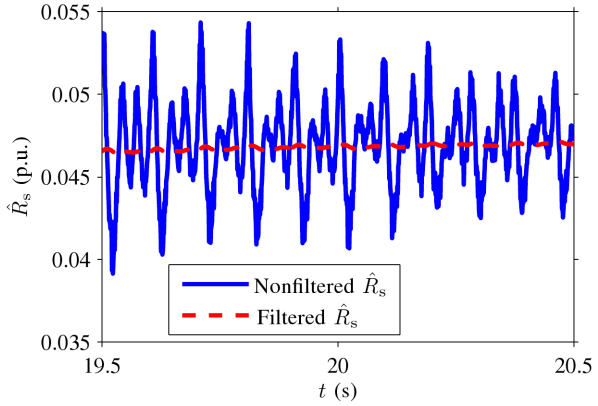

Fig. 9. Behaviour of the resistance estimate, when $\hat{\omega}_\mathrm{m} \approx -0.05$ p.u. in Fig. 8(b). The solid line is the actual estimate $\hat{R}_\mathrm{s}$ and the dashed line is the filtered estimate $\hat{R}_\mathrm{sf}$.

C. Linearized Models

1) Inductance Adaptation: The nonlinear estimation-error dynamics consisting of (46) – (49) are linearized. When the d-axis inductance is adapted, the resulting fifth-order linearized system is given in (53), where

$$a_{13}=-k_{11}\beta_\mathrm{num}-k_{12}\beta_\mathrm{den},\quad a_{23}=-k_{21}\beta_\mathrm{num}-k_{22}\beta_\mathrm{den}$$
$$a_{41}=d\frac{k_{21}-\hat{\omega}_\mathrm{m}}{(\hat{L}_\mathrm{d}-\hat{L}_\mathrm{q})i_\mathrm{d}},\quad a_{42}=\frac{e+k_{22}d}{(\hat{L}_\mathrm{d}-\hat{L}_\mathrm{q})i_\mathrm{d}}$$
$$a_{43}=\frac{da_{23}-e\beta_\mathrm{den}}{(\hat{L}_\mathrm{d}-\hat{L}_\mathrm{q})i_\mathrm{d}},\quad a_{44}=-d\frac{\tilde{\psi}_{\mathrm{d}0}+\beta_\mathrm{den}}{(\hat{L}_\mathrm{d}-\hat{L}_\mathrm{q})i_\mathrm{d}}$$
$$a_{45}=-d\frac{i_\mathrm{q}}{(\hat{L}_\mathrm{d}-\hat{L}_\mathrm{q})i_\mathrm{d}}$$

and

$$\beta_{\mathrm{den}} = (L_{\mathrm{d}} - L_{\mathrm{q}})[i_{\mathrm{d}}\cos(2\tilde{\vartheta}_{\mathrm{m0}}) - i_{\mathrm{q}}\sin(2\tilde{\vartheta}_{\mathrm{m0}})]$$
$$\beta_{\mathrm{num}} = (L_{\mathrm{d}} - L_{\mathrm{q}})[i_{\mathrm{q}}\cos(2\tilde{\vartheta}_{\mathrm{m0}}) + i_{\mathrm{d}}\sin(2\tilde{\vartheta}_{\mathrm{m0}})]$$

For design purposes, the order of the system is reduced by assuming the speed-adaptation loop to be much faster than the dynamics of the flux observer and the inductance-adaptation loop. Hence, the speed adaptation can be considered to be in quasi-steady state, corresponding to $\tilde{i}_{\mathrm{q}} = 0$ and further $\tilde{\psi}_{\mathrm{q}} = i_{\mathrm{d}}(L_{\mathrm{d}} - L_{\mathrm{q}})\tilde{\vartheta}_{\mathrm{m}}$. Using this condition, (53) reduces to

$$\frac{\mathrm{d}}{\mathrm{d}t}\begin{bmatrix}\tilde{\psi}_{\mathrm{d}}\\ \tilde{\psi}_{\mathrm{q}}\\ \tilde{L}_{\mathrm{d}}\end{bmatrix} = \begin{bmatrix}k_{11} & k_{12}+\hat{\omega}_{\mathrm{m}} & -k_{11}i_{\mathrm{d}}\\ k_{21}-\hat{\omega}_{\mathrm{m}} & k_{22} & -k_{21}i_{\mathrm{d}}\\ k_{\mathrm{L}} & -k_{\mathrm{L}}\beta & -k_{\mathrm{L}}i_{\mathrm{d}}\end{bmatrix}\begin{bmatrix}\tilde{\psi}_{\mathrm{d}}\\ \tilde{\psi}_{\mathrm{q}}\\ \tilde{L}_{\mathrm{d}}\end{bmatrix} \quad (54)$$

where $\tilde{\vartheta}_{\mathrm{m0}} = 0$ is assumed. The characteristic polynomial of this system is given in (18). In a similar manner, the linearized estimation-error dynamics are obtained for the adaptation of the q-axis inductance:

$$\frac{\mathrm{d}}{\mathrm{d}t}\begin{bmatrix}\tilde{\psi}_{\mathrm{d}}\\ \tilde{\psi}_{\mathrm{q}}\\ \tilde{L}_{\mathrm{q}}\end{bmatrix} = \begin{bmatrix}k_{11} & k_{12}+\hat{\omega}_{\mathrm{m}} & -k_{12}i_{\mathrm{q}}\\ k_{21}-\hat{\omega}_{\mathrm{m}} & k_{22} & -k_{22}i_{\mathrm{q}}\\ k_{\mathrm{L}} & -k_{\mathrm{L}}\beta & k_{\mathrm{L}}\beta^2 i_{\mathrm{d}}\end{bmatrix}\begin{bmatrix}\tilde{\psi}_{\mathrm{d}}\\ \tilde{\psi}_{\mathrm{q}}\\ \tilde{L}_{\mathrm{q}}\end{bmatrix} \quad (55)$$

2) Resistance Adaptation: When the speed-adaptive full-order observer is augmented with the low-pass filter (31) and the stator-resistance adaptation law (34), the linearized estimation-error dynamics are governed by the sixth-order system (56). In order to reduce the order of the system, it is assumed that the speed-adaptation loop is faster than the flux observer and the resistance-adaptation loop, i.e. $\tilde{\psi}_{\mathrm{q}} = i_{\mathrm{d}}(L_{\mathrm{d}} - L_{\mathrm{q}})\tilde{\vartheta}_{\mathrm{m}}$. Under this assumption, (56) reduces to (57). The characteristic polynomial of (57) is given in (36).

REFERENCES

[1] E. Capecchi, P. Guglielmo, M. Pastorelli, and A. Vagati, "Position-sensorless control of the transverse-laminated synchronous reluctance motor," *IEEE Trans. Ind. Appl.*, vol. 37, no. 6, pp. 1768–1776, Nov./Dec. 2001.

[2] H. F. Hofmann, S. R. Sanders, and A. EL-Antably, "Stator-flux-oriented vector control of synchronous reluctance machines with maximized efficiency," *IEEE Trans. Ind. Electron.*, vol. 51, no. 5, pp. 1066–1072, Oct. 2004.

[3] S.-C. Agarlită, I. Boldea, and F. Blaabjerg, "High-frequency-injection-assisted "active flux"-based sensorless vector control of reluctance synchronous motors, with experiments from zero speed," *IEEE Trans. Ind. Appl.*, vol. 48, no. 6, pp. 1931–1939, Nov./Dec. 2012.

[4] J.-I. Ha, S.-J. Kang, and S.-K. Sul, "Position-controlled synchronous reluctance motor without rotational transducer," *IEEE Trans. Ind. Appl.*, vol. 35, no. 6, pp. 1393–1398, Nov./Dec. 1999.

[5] A. Consoli, F. Russo, G. Scarcella, and A. Testa, "Low- and zero-speed sensorless control of synchronous reluctance motors," *IEEE Trans. Ind. Appl.*, vol. 35, no. 5, pp. 1050–1057, Sep./Oct. 1999.

[6] H. W. de Kock, M. J. Kamper, O. C. Ferreira, and R. M. Kennel, "Position sensorless control of the reluctance synchronous machine considering high frequency inductances," in *Proc. PEDS 2007*, Bangkok, Thailand, Nov. 2007, pp. 812–821.

[7] M. Schroedl and P. Weinmeier, "Sensorless control of reluctance machines at arbitrary operating conditions including standstill," *IEEE Trans. Power Electron.*, vol. 9, no. 2, pp. 225–231, Mar. 1994.

[8] R. Morales-Caporal and M. Pacas, "Encoderless predictive direct torque control for synchronous reluctance machines at very low and zero speed," *IEEE Trans. Ind. Electron.*, vol. 55, no. 12, pp. 4408–4416, Dec. 2008.

[9] T. Matsuo and T. A. Lipo, "Rotor position detection scheme for synchronous reluctance motor based on current measurements," *IEEE Trans. Ind. Appl.*, vol. 31, no. 4, pp. 860–868, July/Aug. 1995.

[10] M.-Y. Wei and T.-H. Liu, "A high-performance sensorless position control system of a synchronous reluctance motor using dual current-slope estimating technique," *IEEE Trans. Ind. Electron.*, vol. 59, no. 9, pp. 3411–3426, Sept. 2012.

[11] A. Piippo, M. Hinkkanen, and J. Luomi, "Sensorless control of PMSM drives using a combination of voltage model and HF signal injection," in *Conf. Rec. IEEE-IAS Annu. Meeting*, vol. 2, Seattle, WA, Oct. 2004, pp. 964–970.

[12] O. Wallmark, L. Harnefors, and O. Carlson, "An improved speed and position estimator for salient permanent-magnet synchronous motors," *IEEE Trans. Ind. Electron.*, vol. 52, no. 1, pp. 255–262, Feb. 2005.

[13] A. Piippo, M. Hinkkanen, and J. Luomi, "Adaptation of motor parameters in sensorless PMSM drives," *IEEE Trans. Ind. Appl.*, vol. 45, no. 1, pp. 203–212, Jan./Feb. 2009.

[14] W. Hammel and R. M. Kennel, "Position sensorless control of PMSM by synchronous injection and demodulation of alternating carrier voltage," in *Proc. IEEE SLED 2010*, Padova, Italy, July 2010, pp. 56–63.

[15] M. Ranta and M. Hinkkanen, "Online identification of parameters defining the saturation characteristics of induction machines," *IEEE Trans. Ind. Appl.*, vol. 49, no. 5, pp. 2136–2145, Sep./Oct. 2013.

[16] G. Yang, R. Tomioka, M. Nakano, and T. H. Chin, "Position and speed sensorless control of brushless DC motor based on an adaptive observer," *IEEJ Trans. Ind. Appl.*, vol. 113, pp. 579–586, May 1993.

[17] A. Piippo, M. Hinkkanen, and J. Luomi, "Analysis of an adaptive observer for sensorless control of interior permanent magnet synchronous motors," *IEEE Trans. Ind. Electron.*, vol. 55, no. 2, pp. 570–576, Feb. 2008.

[18] T. Tuovinen, M. Hinkkanen, L. Harnefors, and J. Luomi, "Comparison of a reduced-order observer and a full-order observer for sensorless synchronous motor drives," *IEEE Trans. Ind. Appl.*, vol. 48, no. 6, pp. 1959–1967, Nov./Dec. 2012.

[19] L. Harnefors and H.-P. Nee, "A general algorithm for speed and position estimation of AC motors," *IEEE Trans. Ind. Electron.*, vol. 47, no. 1, pp. 77–83, Feb. 2000.

[20] M. J. Corley and R. D. Lorenz, "Rotor position and velocity estimation for a salient-pole permanent magnet synchronous machine at standstill and high speeds," *IEEE Trans. Ind. Appl.*, vol. 34, no. 4, pp. 784–789, Jul./Aug. 1998.

[21] T. Tuovinen and M. Hinkkanen, "Adaptive full-order observer with high-frequency signal injection for synchronous reluctance motor drives," in *IEEE J. Emerg. Sel. Topics Power Electron.*, in press

[22] W. T. Villet, M. J. Kamper, P. Landsmann, and R. Kennel, "Evaluation of a simplified high frequency injection position sensorless control method for reluctance synchronous machine drives," in *Proc. IET PEMD 2012*, vol. 1, Bristol, UK, Mar. 2012, pp. 1–6.

[23] J. K. Pedersen, F. Blaabjerg, J. W. Jensen, and P. Thogersen, "An ideal PWM-VSI inverter with feedforward and feedback compensation," in *Proc. EPE'93*, vol. 4, Brighton, U.K., Sept. 1993, pp. 312–318.

[24] J. Choi and S. Sul, "Inverter output voltage synthesis using novel dead time compensation," *IEEE Trans. Power Electron.*, vol. 11, no. 2, pp. 221–227, Mar. 1996.

[25] L. Harnefors, "Design and analysis of general rotor-flux-oriented vector control systems," *IEEE Trans. Ind. Electron.*, vol. 48, no. 2, pp. 383–390, Apr. 2001.

[26] Z. Qu, T. Tuovinen, and M. Hinkkanen, "Inclusion of magnetic saturation in dynamic models of synchronous reluctance motors," in *Proc. ICEM'12*, Marseille, France, Sept. 2012, pp. 994–1000.

Toni Tuovinen received the M.Sc. degree from University of Helsinki, Helsinki, Finland, in 2005, and the M.Sc.(Eng.) degree from Helsinki University of Technology, Espoo, Finland, in 2009.

Since 2007, he has been with Helsinki University of Technology (part of Aalto University, Espoo, since 2010). He is currently a Research Scientist with the Department of Electrical Engineering, Aalto University. His main research interest is the control of electric drives.

Marko Hinkkanen (M'06–SM'13) received the M.Sc.(Eng.) and D.Sc.(Tech.) degrees from Helsinki University of Technology, Espoo, Finland, in 2000 and 2004, respectively.

Since 2000, he has been with Helsinki University of Technology (part of Aalto University, Espoo, since 2010). He is currently an Assistant Professor with the Department of Electrical Engineering, Aalto University. His research interests include electric drives and electric machines.